Development of a four-parameter phenomenological model for the nonlinear viscoelastic behaviours of magnetorheological gels

Shaoqi Li[a], Tingting Tian[b], Huixing Wang[c] ,Yancheng Li[a,d*], Jianchun Li[a,b] , Yadong Zhou[b] and Jinbo Wu[e]

[a] *School of Civil and Environmental Engineering, University of Technology Sydney, Ultimo 2007, Australia*

[b] *School of Civil Engineering, Tianjin Chengjian University, Tianjin 300384, People's Republic of China*

[c] *School of Mechanical Engineering, Nanjing University of Science and Technology, Nanjing 210094, People's Republic of China*

[e]*Materials Genome Institute, Shanghai University, People's Republic of China*

Abstract

Magnetorheological gel (MRG) excels in the material properties in term of adjustability and sedimentation performance, which could upgrade the performances of the current magnetorheological fluid based adjustable devices for structural control and vibration mitigation. However, the characterization and modelling of the stress-strain hysteresis responses of MRG has not been reported in the past, which are fundamental steps toward engineering applications. In this study, the stress-strain hysteresis of polyurethane based MR gel sample with 60% carbonyl iron particle weight fraction was characterised under sinusoidal shear excitations with broad ranges of strain amplitude (5%–100%), excitation frequency (0.1 Hz–2 Hz) and magnetic fields (0–0.91 T). Significant stress overshooting phenomenon were observed under the application of low magnetic fields (0.27 T). A structurally-simple and accurate phenomenological model has been established to capture this unique nonlinearity. By validating the experimental results, the proposed model accurately predicts the hysteretic behaviour and the overshoot of the MRG under the excitation scenarios and the magnetic fields considered. Finally, the support vector machine (SVM) was implemented to provide the solution to the model generalization. The SVM-assisted model showed good agreement with the experimental data and can benefit the efficiency and viability in developing controllable MRG-based devices and system.

Keywords

Magnetorheological gel, Material characterisation, Hysteresis modelling, Dynamic properties, Stress overshoot, Support vector machine

1. Introduction

Magnetorheological gel (MRG), as a new branch of magnetorheological (MR) materials [1-4], holds the potential to be adopted in adjustable devices, due to that it offers extensive adjustability in material properties under the influence of the external magnetic field [5]. The compositions of MRG are typically polymer gel as the matrix, ferromagnetic filling particles, and additives. Compared with the free-flowing liquid matrix of MR fluid, which is the most reported controllable fluid, the partially entangled polymer gel matrix has a higher viscosity and yield stress, which decides the lower sedimentation behaviour and superior sealing performance of MRG [6, 7]. Moreover, the properties of the polymer matrix can be simply orchestrated by changing the concentration of copolymer, morphology, and cross-link profile; and, depending on the fabrication composition and fabrication process, MRGs appear as soft gel, and solid-like [8-12]. Therefore, the availability of the controllable materials for adjustable devices can be greatly expanded, and the performance and adjustability of the controllable devices can be more precisely designated and tailored.

Being classified as both MR material and complex fluid, MRG express strong dependencies on both magnetic fields and excitation inputs, i.e., strain amplitude and strain rate (or excitation frequency) [13]. Furthermore, adaptive devices are normally subjected to reciprocating loadings with large strain amplitudes, which generally lead to highly nonlinear stress-strain hysteresis. Under the application of the external magnetic field, the nonlinearity in the hysteretic behaviour becomes more drastic and complicated since the materials transform from gel-like liquid state, more sticky elastomeric material to solid materials. Essential efforts were made to establish understandings of this novel controllable complex fluid and mainly focused on reporting the innovative recipes for high adjustable material, experimental testing to revealing the rheological behaviour and material stability [14-16]. The adjustability of yield stress from about 10 kPa to almost 200 kPa can be achieved by MRG under the influence of the external magnetic field [17]. From the application perspective, the high storage modulus and adjustability of MRG can contribute to a more compact device design and higher controllable ranges of the device. No particle sedimentation was observed in MRG if the solvent content is lower than 25 wt% [14]. These findings suggested the potentials of developments of compact and stable controllable devices for various engineering prospects, including controllable damping devices and torque transmission actuators.

Towards the design of controllable-material-based devices and predicting the performance of the devices, it is an essential step to conduct characterization of the stress-strain hysteresis behaviour of the material. The common approach to obtain the stress-strain relationships for MR materials is performing sinusoidal shear tests using customised shear test rigs [1, 18, 19] or rheometers [20, 21] under different levels of magnetic fields. Commercial rheometers are widely merited for its simple set up and high precision for rheology studies and material characterisations. The raw waveform data recording function for large amplitude oscillatory shear test and the electromagnet accessories enable the stress-strain hysteresis characterisation for MR materials. However, the hysteresis behaviour of MRG has not been characterized in the previous research.

Substantial efforts have been made on the modelling of other controllable materials to predict the stress-strain hysteresis loop under different excitation inputs and external magnetic field [22, 23]. These models were developed and can be adopted in the control algorithms to achieve active or semi-active control devices and systems for both engineering practices and numerical simulations. Two general types of models can be classified from the past investigations are physical model and phenomenological model. The physical models are constructed based on the interpretation of the microstructure of the material and generally have over-simplified assumptions and require a sophisticated computation process [24-26]. On the other hand, phenomenological models are based on the empirical relations between the excitation inputs and hysteresis performances. They provide a versatile and straightforward model formulation process and consider the dependencies of frequency, strain amplitude, and external magnetic field. Commonly, the accuracy and simplicities of the model, i.e., less parameter and avoiding piecewise function and differential equations, significantly contribute to the effectiveness and response time of the controller [27].

Therefore, phenomenological models are extensively adopted in depicting the hysteresis responses of controllable materials and devices. Li et al. [21] proposed a four-parameter viscoelastic model for the prediction of dynamic hysteresis responses of MREs. Dargahi et al. [18] established a Prandtl-Ishlinskii model with the sound performance of describing the dependencies of the field and excitation inputs for MRE. Yu et al. [28] constructed a Bouc-Wen-operator-based hysteresis model, which can capture the strain stiffening of the MRE base isolator under the influence of the applied external magnetic field. For controllable-fluid-based applications, Spencer et al. [29] proposed a simple Bouc-Wen model for the semiactive control of MRF dampers for engineering structures. In light of this successful implementation of Bouc-

Wen model in MRF dampers, this model has been modified to further extend its applicability for large scale damper [30], self-centering bracing [31] and MRE base isolators [32]. Although numerous variations of phenomenological models have been formulated to capture the stress-strain hysteresis for magnetorheological materials, their applications to MRG has never been reported.

In this study, the MRG sample with carbonyl iron particle (CIP) content of 60 wt% was prepared. The dynamic hysteresis responses of the MRG sample have been characterized using a rheometer under sinusoidal shear excitations with broad ranges of strain amplitude (10% – 100%), excitation frequency (0.1 Hz – 2 Hz) and magnetic field (0 – 0.91 T). The experiments suggested that the dynamic behaviour of MRG heavily depends on the excitation inputs and magnetic fields. In particular for low level of field (0.27 T), stress overshoot phenomenon occurred at the reverse of the shear flow. A Bouc-Wen model was implemented to fit the characterised stress-strain behaviour of MRG however failed in predicting the overshoot phenomenon. A simple and accurate phenomenological model with only four parameters has therefore been proposed to capture this unique nonlinearity of MRG, and the field-induced stress overshoot. For the generalisation purpose, the parameters of the proposed model are identified form the experimental data and used for the training of a support vector (SVM) assisted model. The SVM assisted model was validated with other group of experimental data showed accurate predictions of the hysteretic behaviour and overshoot of the MRG under all excitation scenarios and the magnetic fields considered.

2. Experimental

2.1 *Material preparation*

The MRG sample in this research is fabricated with 60 wt% of CIP (spherical, 3.5 μ diameter, provided by Beijing Xing Rong Yuan Technology Co., Ltd., China) and polyurethane (4608 oil-based polyurethane, provided by Jining Tainuo Chemical Co., Ltd., China). Polyurethane is normally synthesized by toluene diisocyanate and polypropylene glycol; and its viscosity can be easily tailored by the ratio between the diisocyanate and glycol. Higher diisocyanate concentration gives higher viscosity of the polyurethane [14, 15]. The polyurethane appears as soft gel state and has an amber hue before mixing. To prepare the MRG, firstly, the polyurethane sample was stirred at 60 ˚C for 30 minutes with the mixer set at 500 rpm. Then the polyurethane was cooled down to 30 ˚C. The weighted CIP was added to the polyurethane and mixed for 1 hour at 500 rpm. Then, the mixture was treated with an ultrasonic vibrator for 15 minutes to get a more uniform distribution of CIP and remove the air bubble in the mixture. To further eliminate the air bubble and moisture, the mixture was stored in the vacuum drying machine for 2 hours and then placed 2 days at room temperature. Finally, the MRG with CIP of 60 wt% was prepared. Figure 1(a) is the photo of the prepared MRG sample settled in the beaker. In figure 1(b), as beaker is tilted, the MRG surface bulges towards the tilting direction. Then the MRG surface gradually levels to the horizontal plane under the influence of gravity after approx. 15 seconds, as presented in figure 1(c). This behaviour suggests that MRG has the higher stability and viscosity, compared with free flowing MRF; however, yet reached the elastomeric state as MRE.

(a)

(b)

(c)

Figure 1. Photos of the MRG sample (a) settled in the beaker; (b) the beginning of the tilting; (c) approx. 15 seconds after tilting

143

144 2.2 *Experimental setup and measurements*

145 The dynamic hysteresis characterization of the MRG sample was performed on the MCR 302
146 rheometer (Physica MCR 302, Anton Paar Co., Austria) with the parallel plate measurement
147 system (PP20, Anton Paar Co., Austria), as presented in figure 2(a). The rheometer is equipped
148 with the raw data module which enables the recording of raw stress and strain waveforms. The
149 parallel plate measurement system has a uniform gap height between the PP20 measuring tool
150 and the base plate, thus yields a uniform magnetic field distribution in the gap. In all
151 experiments, the gap was set at 1 mm. Since the radius of the PP20 measuring tool is 10 mm,
152 the volume of MRG sample controlled for each test is $\pi \times 1^2 \times 0.1 = 0.314$ ml. The MRG sample
153 is applied at the centre of the base plate in the gap. The magnetic field in the gap was controlled
154 by the coil sets embedded under the rheometer bottom plate. The maximum current applied to
155 the coils is 5A by the power supply (PS-MDR/5A, Anton Paar Co., Austria). To find the
156 correlation between the fiend density and the applied current and to assess the homogeneity of
157 the magnetic field, the magnetic fields at three locations beneath the base plate were measured
158 by a teslameter (FH54, Magnetic Physics Inc., Germany) with a hall probe (HS-TGB5,
159 Magnetic Physics Inc., Germany) inserted under the base plate at the centre, as illustrated in
160 figure 2(b) and (c). The three locations are the projections of the centre, middle of the radius
161 (5 mm from the centre) and the edge (10 mm from the centre) of the PP20 measurement plate.
162 During the measurement, 0 A to 5 A (1 A step) currents were applied to the coil; and, MRG
163 sample was applied to the centre of the base plate with the gap height set at 1 mm. Since the
164 hall probe cannot be accommodated inside of the gap when sample was placed, the probe
165 inserted in the slot beneath the base plate. The measured correlation between the field density
166 and the applied current is presented in Table 1. Small discrepancies in the field densities at the
167 three locations were observed, around 5%. The average of the field density at the three locations
168 was used in the following sections to indicate the levels of magnetic fields. When the current
169 is increased from 0 to 5 A, the magnetic field density increases almost linearly from 0 T to 0.91
170 T.

171

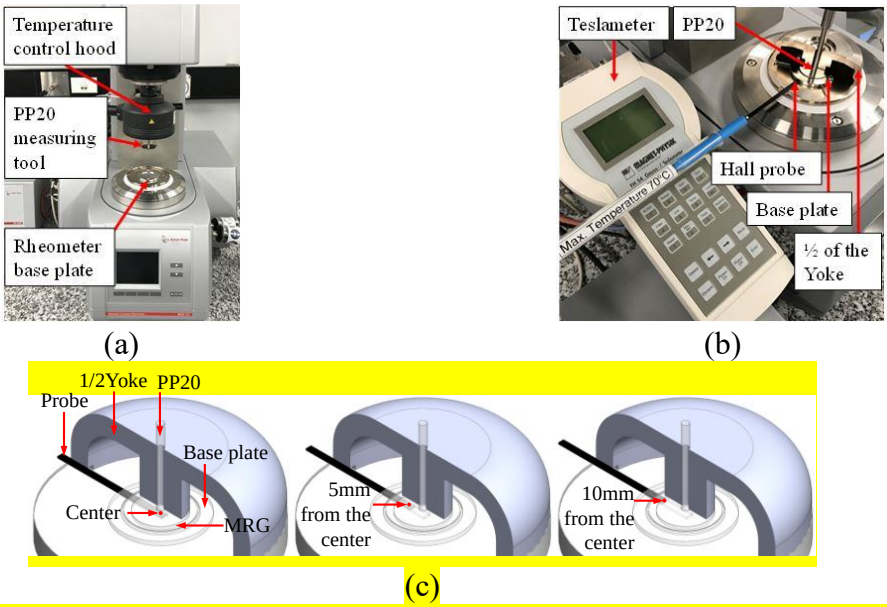

Figure 2. Set up of (a) characterization tests; (b) measurement of magnetic field; (c) locations of field measurement

172

Table 1. Correlation between the magnetic field density and applied current

Current (A)	Centre (T)	5mm from centre (T)	10mm from centre (T)	Average (T)
0	0	0	0	0
1	0.26	0.26	0.28	0.27
2	0.47	0.46	0.49	0.47
3	0.64	0.62	0.66	0.64
4	0.78	0.77	0.80	0.79
5	0.90	0.88	0.93	0.91

During the measurement of magnetic field and characterisation tests, a set of magnetic chambers (MDR H-PTD 200, Anton Paar Co., Austria) were placed on the rheometer base plate to form an enclosed magnetic flux path. The temperature was controlled at 25 ± 0.2 ˚C for all measurements by a temperature module (C-PTD 200, Anton Paar Co., Austria) connected to the base plate and a temperature control hood (H-PTD 200 hood, Anton Paar Co., Austria) applied over the magnetic chamber. It should be noted that the temperature fluctuations vary with the applied current. By applying 0, 1, and 2 A currents for 300 seconds, the temperature increment can be well limited within 0.03 ˚C. At 3, 4, and 5 A, the temperature increases for 0.05, 0.12 and 0.19 ˚C over 300 seconds, respectively. From the past research [33, 34], such level of temperature increment only decreases the dynamic yield stress of polymer-based MR materials by less than 0.15%. In this research, the testing time is controlled under 300 seconds which allows 30 cycles of 0.1 Hz test.

The characterisation tests of the hysteresis responses of the MRG were conducted under strain-controlled sinusoidal excitations with various frequencies, strain amplitudes and magnetic fields considered. To date, such characterisation has yet to be reported for MRG. For controllable fluid like MRF, its hysteresis behaviour has normally been characterised under excitation frequency from 0.5 Hz to 1.5 Hz [35]. In this research, a wider range of frequency was considered for MRG, which were 0.1, 0.5, 1 and 2 Hz. The strain amplitudes for the measurements were set from 10% to 100%. Measurements of each excitation input were carried out with six levels magnetic field applied (currents applied to the coil set: 0, 1, 2, 3, 4, 5 A), since the storage modulus reaches the maximum when the magnetic field density increased to about 0.8 T [14]. All tests were conducted under stain control. The temperature was set at 25 ˚C for all tests. 513 data points were samples for each measured hysteresis loop.

2.3 *MRG dynamic characteristics*

The recorded stress-strain hysteresis of the MRG sample indicated strong and complicated dependencies on excitation frequency, strain amplitude, and the external magnetic field. Figure 3 shows the stress-strain relationships of the MRG sample under the influences of the frequency, strain amplitude, and magnetic field. The enclosed area of the hysteresis loop represented the dissipated energy under the sinusoidal shear motion. The stiffness can be represented by the slope of the major axis of the hysteresis curve. Primarily, the increases of excitation frequency, strain amplitude and magnetic field contributes to both the energy dissipation and stiffness of MRG. The presence and intensifying of the external field form and strengthen the CIP chain structures in the gel matrix and result in the drastic growth of the elastic component in the MRG. The dynamic response of MRG is similar to pure viscous material without the magnetic field; however, under the magnetic fields, it become to be ellipse shaped as the viscoelastic materials. This unique transition from the magnetic field off and on states of MRG differs from other MR materials like MRF and MRE. MRF and MRE exhibit box-shaped and ellipse-shaped hysteresis loops, respectively [18, 35]; and, the presence of external field does not change the

general outlines of their hysteresis loops. An apparent stress overshoot effect was observed and will be discussed in the following section.

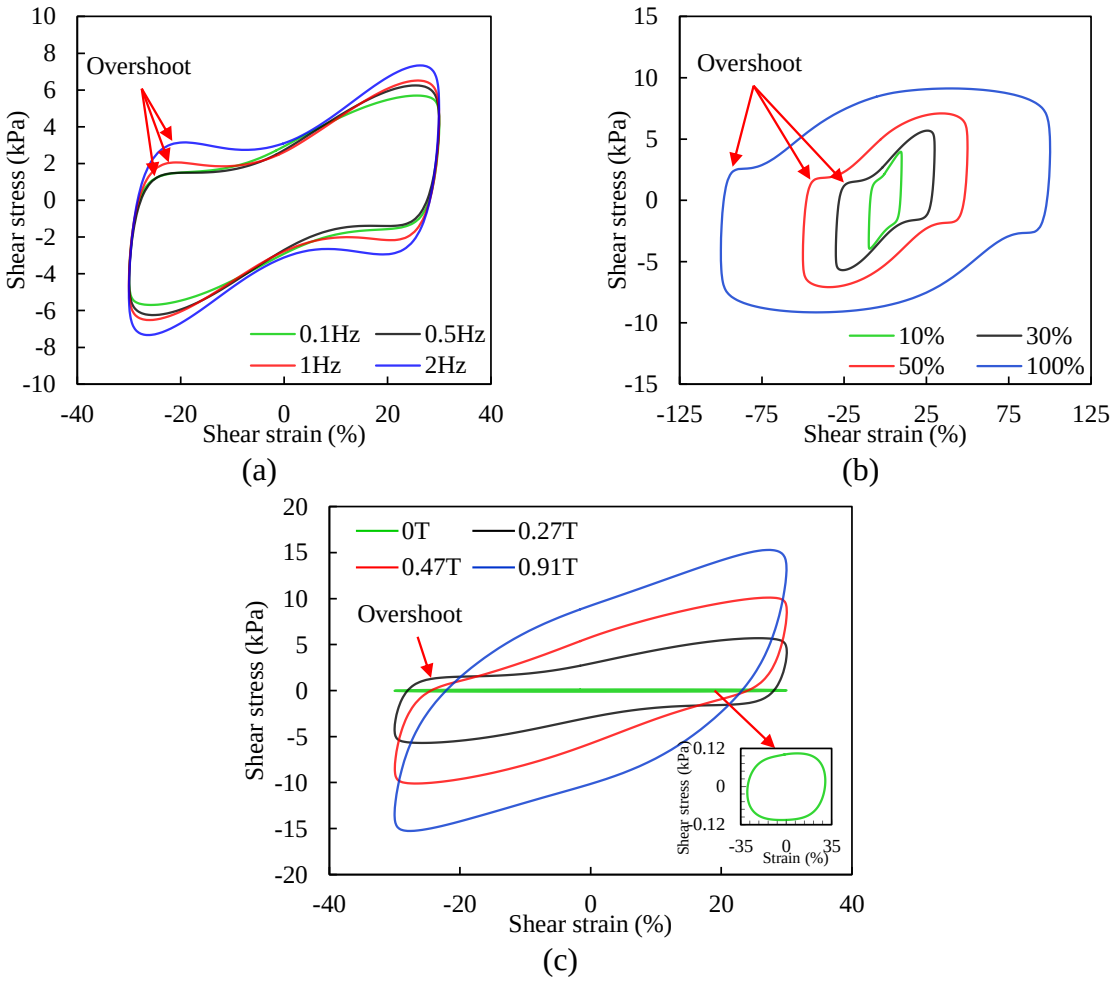

Figure 3. Hysteretic responses of MRG (a) influence of frequency (30% strain; 0.27 T); (b) influence of strain amplitude (0.1 Hz; 0.27 T); (c) influence of magnetic field (0.1 Hz; 30% strain).

Figure 3(a) compares the influence of excitation frequency on the stress-strain responses of MRG when strain amplitude is fixed at 30% and 1 A current applied to the coil. The growing frequency effectively increased the dissipated energy and the stiffness of the MRG. This phenomenon is in line with the findings from Yang et al. [6] and Xu et al. [14]. Figure 3 (b) represents the hysteresis loop with different strain amplitudes applied under the same level of excitation frequency (0.1 Hz) and magnetic field (0.27 T). Although the increase of strain amplitude increases the measured maximum shear stress, the reducing slope indicates a decreasing trend of storage modulus with the rise of strain amplitude. Similar results were reported in [15, 36]. Figure 3(c) depicts the influence of the applied magnetic field when the excitation inputs are fixed at 0.1 Hz and 30% strain. The plot for the 0 T scenario, located at the bottom right corner of Figure 3(c), has a nearly circular shape, and the gradual slope of the hysteresis loop suggested a minor effect of elasticity. Due to the absence of the magnetic field, CIP contents are randomly distributed in the polyurethane matrix rather than forming columnar structures [16, 37]. The application of the external magnetic field results in a nonlinear viscoelastic-material-like behaviour. Further intensifying the magnetic field (up to 0.91 T) outputs an increasing trend of both stiffness and energy loss of MRG under the sinusoidal waveform.

Furthermore, significant stress overshooting phenomenon can be observed at the shear rate reversing points of a strain cycle, only under the application of magnetic field, especially for the lower-level magnetic fields (0.27 T). The occurrence of overshooting is because of that the reversed strain deformation is accumulated slower than the unloading of shear stress [38]. Numerous similar stress-strain responses were reported in the rheological studies of a wide range of soft matter and complex flow [39-42] and suggested that the occurrence of overshooting is strongly dependent on the strain rate of the shear flow [43]. As suggested by [44], wall slippage and surface roughness of the measurement tool may also lead to stress overshoot phenomenon; and, the overshoot induced by wall slip normally appears as abrupt drop and fluctuation of the shear stress. The smooth and contentious hysteresis loop of MRG means that the measurement is not significantly affected by wall slip.

With the involvement of the magnetic field, the overshoot of MGR is not simply dependent on excitations and shows more unique dependency on the applied current. As shown in figure 3(a) and (b), when 0.27 T applied, this phenomenon showed up in all excitation frequencies and strain amplitudes. Form figure 3(c), although under the same excitation frequency and strain deformation, as the magnetic field further increased to 0.47 T and 0.91 T, the overshoot became less visible and then disappeared. It could be explained that the intensified magnetic field strengthens the yield stress of the CIP chain structures in MRG; the reverse of strain rate occurred before the shear stress reaches the yield level of MRG under a large magnetic field. This phenomenon has not been found in the dynamic characterization studies of other controllable materials.

However, stress overshoot frequently appears in practical engineering applications and is always challenging and critical for researchers to capture in the control system, since the ignorance of overshoot will cause false feedback and failure of control [45, 46]. Thus, modelling practices for MRG were performed in the following section.

3. Modelling of the hysteresis behaviour

3.1 Hysteresis modelling using Bouc-Wen model

As the hysteresis behaviour for MRG has not been revealed in the past, modelling of this unique response is lack of practice and in urgent demand. Here, we use Bouc-Wen model to fit the stress-strain behaviour of MRG since it is the universally-accepted model for portraying nonlinear behaviour of materials and structures, and has been successfully used in reproducing the nonlinear behaviour of MRF/MRE materials and devices [28, 32]. This could be beneficial in modelling for MRG since MRG exhibits both viscous and viscoelastic behaviours depending on the presence of the external magnetic fields. An existing Bouc-Wen model developed by Yang *et al*. for an MRE isolator was implemented to model the MRG dynamic behaviour, with the formulation presented as follow [32]:

$$\begin{aligned} \tau_{\text{est}} &= \alpha k_0 \gamma + (1-\alpha) k_0 z + c_0 \dot{\gamma} \\ \dot{z} &= A\dot{\gamma} - \beta|\dot{\gamma}||z|^{n-1} z - \delta\dot{\gamma}|z|^n \end{aligned} \tag{1}$$

where τ_{est}, γ and $\dot{\gamma}$ are the predicted shear stress, shear strain and strain rate respectively; α, β, δ, A, and n are the non-dimensional parameters which govern the shape and size of the predicted hysteresis loops; k and c are the parameters for the elastic spring and dashpot element, respectively; z is the imaginary variable to represent the time-series function of the shear strain. Generic algorithm was applied to find the combinations of model parameters that yields the minimal value root mean square error (RMSE) between the experimental data and τ_{est}. RMSE can be expressed by Eq. 2 as follow:

$$RMSE = \sqrt{\frac{1}{N}\sum_{j=1}^{N}[\tau(j) - \tau_{\text{est}}(j)]^2} \quad (2)$$

Where N is the number of samples in one hysteresis loop, and $\tau(j)$ and $\tau_{\text{est}}(j)$ stand the j^{th} measured shear stress and the estimated shear stress from the Bocu-Wen model, respectively. The predictions from the Bouc-Wen model are compared with the experimental results in figure 4. Figure 4(a), (b) and (c) presents the fitting of the model under the scenarios of different excitation frequencies, strain amplitudes and applied currents, respectively.

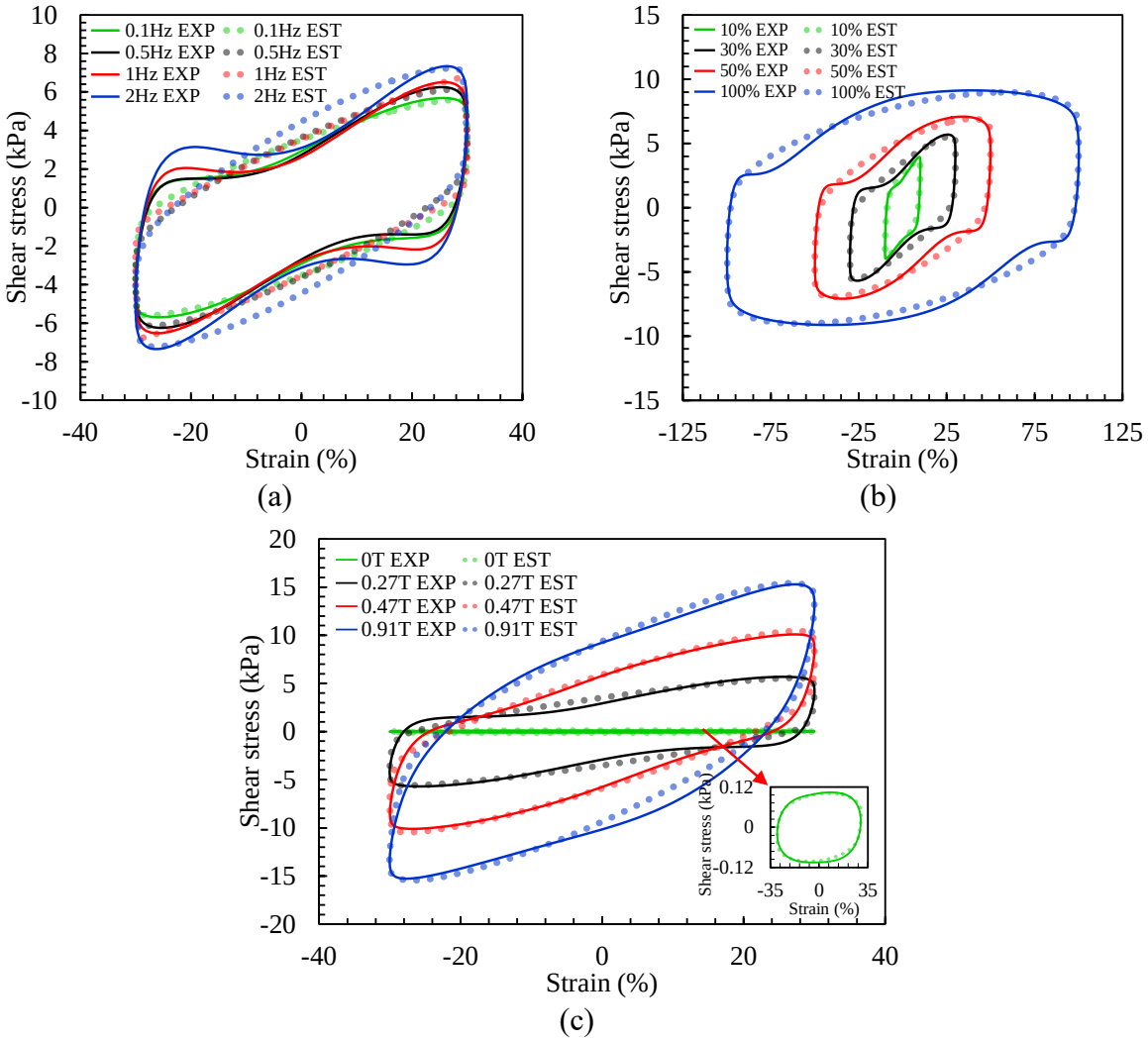

Figure 4. Comparisons between experimental data and simulation result from Bouc-Wen model for: (a) different frequencies, 0.27 T, 30% strain; (b) different strain amplitude, 0.27 T, 0.1 Hz; (c) different magnetic field, 30%, 0.1 Hz.

Overall, the Bouc-Wen model is able to predict the general outlines of the MRG hysteresis loops and the transitions before the revering points of the shear motions; but fails to portrait the overshoot phenomenon after the revise. In figure 4(a) and (b), under 0.27 T scenarios where MRG exhibits significant stress overshot, the Bouc-Wen model ignored all details for the stress overshoot and only estimated shear stress as gradual increasing lines. Although, in figure 4(c), the Bouc-Wen model showed acceptable performances for the viscous-like response under 0 T and the viscoelastic behaviours under 0.47 T and 0.91 T as expected, the ignorance of the overshoot behaviour will still leads to the false feedback for the controller and failure of control

in the application stage. The following sections propose a simple and accurate 4-parameter phenomenological model which can characterize the unique overshoot behaviours of MRG with considering the dependency on the magnetic field to mitigate the lack of practice of MRG hysteresis modelling.

3.2 Formulation of a 4-parameter overshoot model

The experimental results in figure 3 indicated the hysteresis responses of MRG without the application of the magnetic field form an almost circle and barely has the sign of overshoot and elastic behaviour. As the field density increases to 0.27 T, two major features of viscoelasticity and overshoot can be identified. Therefore, when stress overshoot occurred, the shear stress can be decomposed into two parts, which are a viscoelastic part and the overshoot part. In this case, the viscoelasticity part of MRG is modelled by the classic Kelvin-Voigt model, which is the parallel combination of a linear spring element (k) and a viscous dashpot (c) [47]. The Kelvin-Voigt model can be formulated as:

$$\tau_{\text{viscoelastic}} = k\gamma + c\dot{\gamma} \tag{3}$$

where γ is the shear strain and $\dot{\gamma}$ is the shear rate. The overshoot stress (τ_o) component, considering its shape and occurring location, is represented by a two-parameter overshoot element formulated as follow:

$$\tau_o = \begin{cases} (1+\gamma_{\text{nor}})ba^{-a(1+\gamma_{\text{nor}})}, & \dot{\gamma} \geq 0 \\ (1-\gamma_{\text{nor}})ba^{-a(1-\gamma_{\text{nor}})}, & \dot{\gamma} < 0 \end{cases} \tag{4}$$

where b is the governing the magnitude of the overshoot stress component, a is controlling the shape variation and location of the overshoot element, γ_{nor} is the normalized strain (γ). To illustrate the effect of parameter a on the shape and the location of the overshoot stress, the normalized τ_o values are plotted in figure 5. When a value is set at 3, the clear overshoot peak can be observed. With the further increment of a, the peaks start to merge to the shear flow reverse points and become resemblant to the shape and location of the overshoot observed from MRG characterization under the lower magnetic field scenarios. When the a value is lower than 3, the shape of the overshoot element shows a close match with the nonlinear viscoelastic behaviour of the MRG under the higher magnetic fields (0.47 T and 0.91 T). As for 0 T case, where the hysteresis loop presents an almost perfect circular shape, the overshoot element is deactivated (parameter b set as 0). Subsequently, by paralleling the overshoot element with the viscoelasticity model, the proposed model can be formulated as follow:

$$\tau_{\text{est}} = \begin{cases} k\gamma + c\dot{\gamma}, & Applied\ current = 0 \\ k\gamma + c\dot{\gamma} + \tau_o, & Applied\ current \neq 0 \end{cases} \tag{5}$$

where τ_{est} is the estimated shear stress from the proposed model. Figure 6 is the structure of the proposed model. With the combination of the overshoot element and the Kelvin-Voigt model, the estimated shear stress plotted in figure 6 becomes identical to the characterized dynamic behaviour the of MRG with stress overshoot phenomenon.

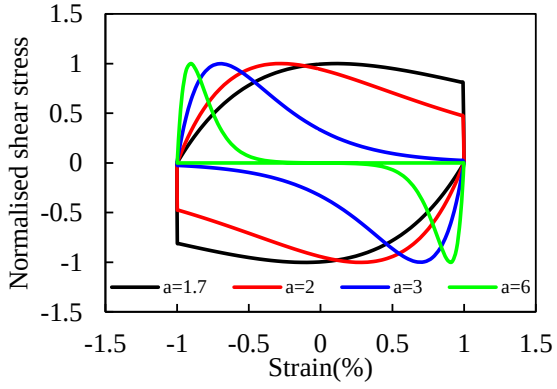

Figure 5. Shape variation of the proposed overshoot element

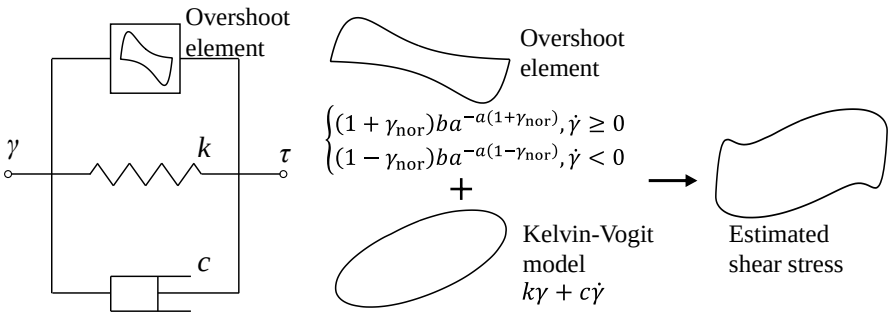

Figure 6. The proposed overshoot phenomenological model

3.3 Parameter identification and analysis

Considering the proposed model contains only four parameters, i.e., *k*, *c*, *a*, and *b*, and has no differential equations, the four parameters can be identified using the least square optimisation method to yield the minimal RMSE (Eq. 2) between the experimental results (τ) and the estimated shear stress (τ_{est}) by the 4-parameter overshoot model. For the 0 T scenarios, *a* values are not considered, and parameter *b* was set to 0 since the overshoot element is only active while the magnetic field is applied. Figure 7 shows the simulation results from the proposed model for scenarios reported in figure 3. In figure 7, the solid and dotted lines represent the experimental data and estimated data by the proposed model, correspondingly. The results suggested that the proposed model accurately captures the hysteresis responses of MRG for all excitation inputs and magnetic fields considered. At the scenarios and locations where the stress overshoot occurred, the model also showed ideal prediction. The full list of simulation results and experimental data are prepared in Appendix.

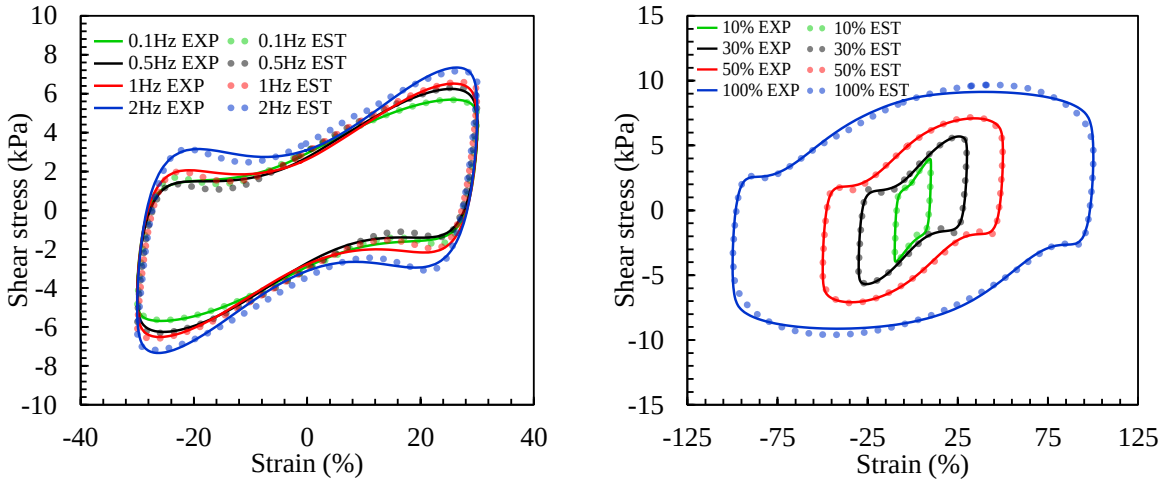

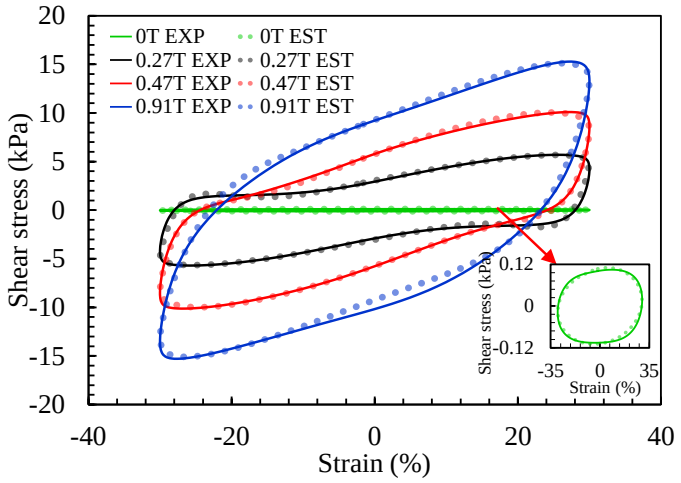

(c)

Figure 7. Comparison between experimental data and simulation result by the proposed overshoot model for: (a) different frequencies, 0.27 T, 30% strain; (b) different strain amplitude, 0.27 T, 0.1 Hz; (c) different magnetic field, 30%, 0.1 Hz.

The identification results of the four parameters are summarised in table 2 (B represents magnetic field density). To further illustrate the relationships between the model parameters and the excitation inputs and the magnetic field, the 3D plots are prepared in figure 8 via Thin Plate Spline algorithm [48]. The clear relationships between the parameter and the variations of the magnetic field and excitation strain amplitude can be observed. In figure 8 (a), the vertical axis represents the magnitude of parameter *a*, which has a clear decreasing trend with the increase of the external magnetic field and with the decrease strain amplitude. At a larger stain amplitude and a lower magnetic field level, *a* value is larger. By comparing *a* values under different excitation frequencies, it can be concluded that *a* decrease with the increase of the frequency. Similarly, in figure 8 (b), parameter *b* also reduces with the intensifying of the magnetic field and the increase of strain amplitude; however, it increases with the increase of the excitation frequency. Corresponding to figure 5, the larger *a* value gives a more marginalized location from the centre of the horizontal axis of the peak of overshoot stress. Moreover, larger *b* value yields a larger stress overshoot magnitude. These trends match closely with the findings from the experiments, suggesting that the lower field density and larger strain amplitude result in a sharper and more significant stress overshoot. For the parameters of the elastic spring (*k*) and the dashpot element (*c*), which are summarised in figure 8 (c) and (d), respectively, they undergo increasing trends with the increase of magnetic field level and the decrease of strain amplitude. The increasing of excitation frequency slightly increases the *k* values; however, it reduces the *c* values. These trends agree with the physical interpretations of the parameters, i.e., the external magnetic field contributes to both the damping and stiffness of the MRG; however, the strain amplitude has the opposite effect on the stiffness and damping.

Table 2. Model parameters *a*, *b*, *k,* and *c* under: (a) 0.1 Hz; (a) 0.5 Hz; (a) 1 Hz; (a) 2 Hz.

(a)

	Amplitude=10%				Amplitude=30%			
B (T)	a	b	k	c	a	b	k	a
0	N/A	0	1.53E-03	8.52E-03	N/A	0	8.70E-04	6.09E-03
0.27	3.57	35.10	3.01E-01	2.71E-01	4.67	70.69	1.68E-01	1.78E-01
0.47	3.44	32.80	5.96E-01	3.62E-01	4.45	64.54	2.92E-01	3.13E-01
0.91	2.63	24.41	8.15E-01	5.12E-01	2.86	51.33	3.28E-01	3.74E-01

	Amplitude=50%				Amplitude=100%			
B (T)	a	b	k	c	a	b	k	a
0	N/A	0	6.75E-04	5.57E-03	N/A	0	5.07E-04	5.03E-03
0.27	6.04	95.54	1.06E-01	1.75E-01	7.27	111.61	5.06E-02	1.42E-01
0.47	4.86	83.25	1.90E-01	2.99E-01	6.00	90.00	8.49E-02	2.30E-01
0.91	2.91	55.70	2.21E-01	3.15E-01	3.02	62.83	1.20E-01	2.36E-01

(b)

	Amplitude=10%				Amplitude=30%			
B (T)	a	b	k	c	a	b	k	a
0	N/A	0	1.89E-03	2.49E-03	N/A	0	1.17E-03	1.86E-03
0.27	3.79	44.38	3.16E-01	6.11E-02	4.46	78.85	1.87E-01	3.31E-02
0.47	3.43	43.56	6.52E-01	9.45E-02	4.27	75.59	3.32E-01	6.83E-02
0.91	3.30	39.52	8.27E-01	1.27E-01	3.73	46.94	3.57E-01	9.64E-02
	Amplitude=50%				Amplitude=100%			
B (T)	a	b	k	c	a	b	k	a
0	N/A	0	7.82E-04	1.72E-03	N/A	0	7.58E-04	1.60E-03
0.27	5.07	98.20	1.29E-01	3.59E-02	5.87	115.77	6.31E-02	3.09E-02
0.47	4.82	81.61	2.16E-01	6.93E-02	5.30	94.36	1.09E-01	5.66E-02
0.91	3.77	62.25	2.29E-01	8.50E-02	4.05	68.08	1.19E-01	6.05E-02

(c)

	Amplitude=10%				Amplitude=30%			
B (T)	a	b	k	c	a	b	k	a
0	N/A	0	2.25E-03	1.14E-03	N/A	0	1.89E-03	9.66E-04
0.27	3.05	20.90	3.29E-01	2.73E-02	4.24	83.06	1.87E-01	1.66E-02
0.47	3.00	19.48	6.79E-01	5.69E-02	4.07	80.16	3.38E-01	3.50E-02
0.91	2.99	17.44	8.91E-01	7.88E-02	3.81	60.68	3.60E-01	4.84E-02
	Amplitude=50%				Amplitude=100%			
B (T)	a	b	k	c	a	b	k	a
0	N/A	0	8.64E-04	9.12E-04	N/A	0	8.42E-04	8.84E-04
0.27	5.26	126.28	1.30E-01	1.78E-02	5.88	145.74	6.64E-02	1.60E-02
0.47	5.17	102.71	2.30E-01	3.46E-02	5.48	120.38	1.12E-01	2.97E-02
0.91	3.72	74.50	2.35E-01	4.14E-02	4.31	84.36	1.22E-01	3.02E-02

(d)

	Amplitude=10%				Amplitude=30%			
B (T)	a	b	k	c	a	b	k	a
0	N/A	0	7.81E-03	2.16E-03	N/A	0	4.92E-03	1.65E-03
0.27	3.44	31.62	3.52E-01	1.78E-02	4.16	90.58	2.13E-01	9.68E-03
0.47	3.31	31.38	6.91E-01	3.45E-02	4.16	91.27	3.69E-01	1.95E-02
0.91	3.06	30.13	9.34E-01	4.03E-02	3.94	84.84	4.32E-01	2.47E-02
	Amplitude=50%				Amplitude=100%			
B (T)	a	b	k	c	a	b	k	a
0	N/A	0	4.25E-03	1.52E-03	N/A	0	3.77E-03	1.39E-03
0.27	4.47	149.98	1.76E-01	9.63E-03	5.23	166.31	8.59E-02	9.87E-03
0.47	4.39	135.18	2.80E-01	1.89E-02	5.14	145.85	1.38E-01	1.74E-02
0.91	4.11	115.96	3.00E-01	2.37E-02	4.16	130.97	1.53E-01	1.89E-02

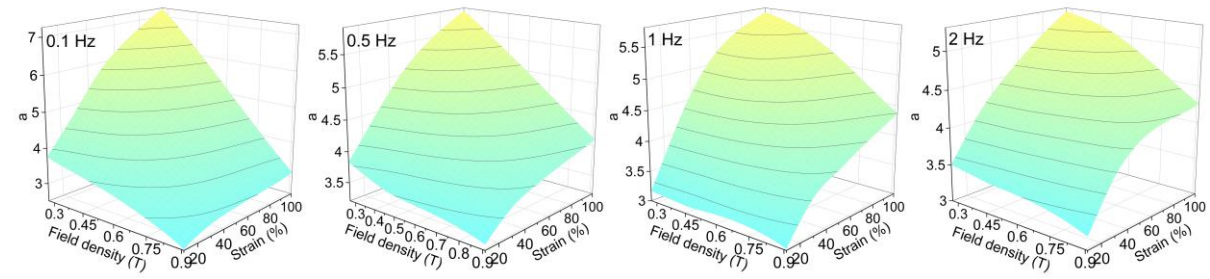

(a)

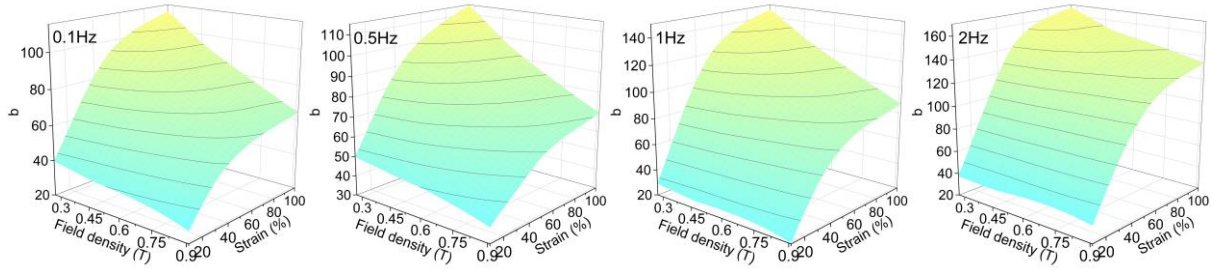

(b)

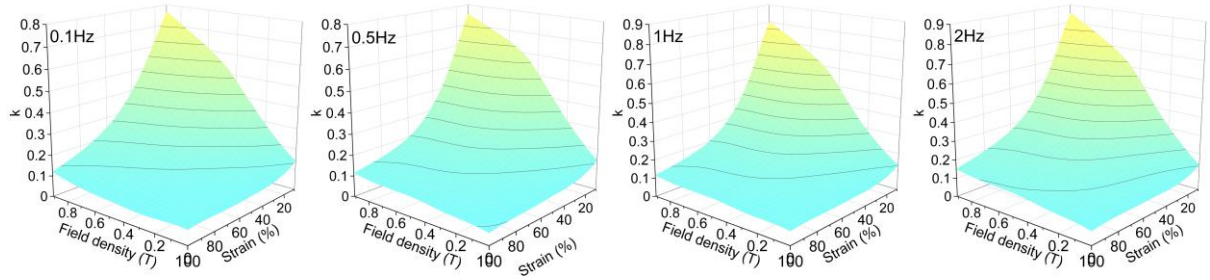

(c)

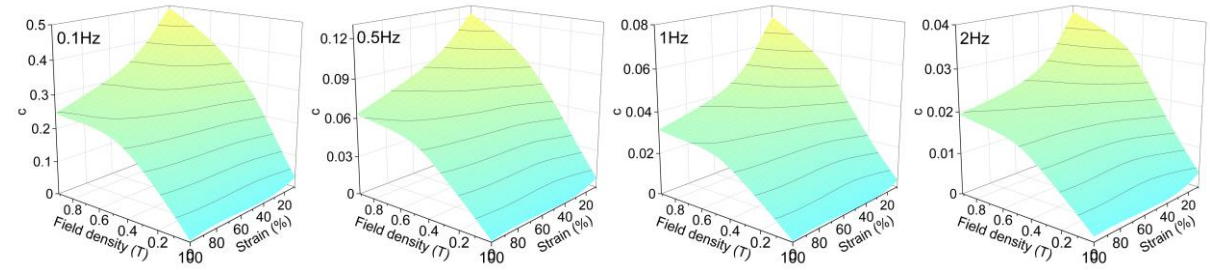

(d)

Figure 8. Model parameter identification results (a) parameter *a*; (b) parameter *b*; (c) parameter *k*; (d) parameter *c*.

To quantitively evaluate the accuracy of the proposed model, mean absolute percentage error (MAPE) was calculated for all cases following:

$$MAPE = \frac{1}{N}\sum_{j=1}^{N} ABS[\frac{\tau(j) - \tau_{\text{est}}(j)}{\tau(j)}] \times 100\% \quad (6)$$

The overall MAPE value of 12.023% suggests that the proposed model can accurately predict the dynamic hysteresis behaviour of MRG under a broad band of excitation strain amplitude, fervency, and different levels of magnetic field.

3.4 Support vector machine (SVM) assisted model

In the practical use of phenomenological models for the controllable materials and devices, the controlling systems are expected to have adaptive performance under fluctuating excitations

and magnetic fields. Since the model parameters are normally identified from experimental characterizations with the test conditions like frequency, amplitude, and magnetic field, held at constant levels, models should be generalised prior to the application in the controlling system. In the past research, model parameters are generally generalized by using the average parameter values under the same magnetic field level and finding the equational expressions between the averaged parameter values and the magnetic field to reduce the complexity of generalization process. This approximation is valid for the scenarios where the material or device performance is majorly dependent on the magnetic field.

However, the characterized MRG dynamic behaviour and the identified model parameters are heavily reliant on both the magnetic field and the excitation inputs. The simplification by averaging parameters does not apply to the MRGs. Moreover, establishing the equational expressions for the parameter values with three variables, i.e., frequency, strain amplitude, and applied magnetic field, is challenging to achieve ideal results.

Support vector machines (SVMs), as supervised learning models, have been successfully implemented in material science and engineering for accurate prediction, classification, and regression analysis [49-52], and can tackle the multi-variable fitting problems in the model generalization process. In this research, an SVM assisted model is formulated as presented in figure 9; and consists of two parts: a trained SVM model and the proposed overshoot phenomenological model. The trained SVM predicts the model parameters, i.e., *a*, *b*, *k*, and *c*, with frequency (*f*), strain amplitude (*A*) and magnetic field density (*B*) as inputs. Subsequently, the proposed phenomenological model uses the parameters predicted by the trained SVM models to produce the estimation of stress-strain hysteresis loops for MRG under the given inputs, i.e., *f*, *A*, and *B*.

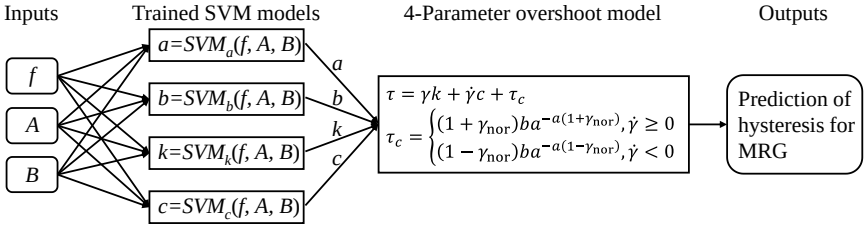

Figure 9. The architecture of the SVM assisted model

In the training process for SVM, the identified values of the four parameters in table 2 were used as training data, which considers frequencies of 0.1, 0.5, 1, and, 2 Hz, strain amplitudes of 10%, 30%, 50%, and 100% and field densities of 0, 0.27, 0.46, and, 0.91 T. The SVM model contains four sub-SVMs for the four model parameters. Radial kernel function was chosen in the four sub-SVMs. For nonlinear data distribution, the kernel function maps the data into higher dimensions to make the distribution more linearly. Two parameters (gamma, and cost) in the kernel function control the fitting of the SVM. Gamma and cost affect the range that the straining samples reach and the penalty for making errors in prediction, respectively. Higher gamma values generate more support vectors and wider reach of data sample. Too large or too small cost will result in poor model predictions by over-fitting or under-fitting, respectively. To achieve optimal prediction accuracy, the gamma and cost values for the kernel function in each sub-SVM were tuned separately until the R-squared value between the estimation and training data reaches a value higher than 0.95. Table 3 summarised the tunned gamma and cost values for the four sub-SVM models. In Figure 10, the estimated parameter values from the trained SVM model and the identified model parameters used in the training were plotted. The overall R^2 value is 0.997 and suggests that the trained SVM provides accurate predictions of all parameters with frequency, amplitude, and, field density are all considered as inputs and can reproduce the hysteresis loops for the test scenarios used for straining process.

Table 3. Gamma and cost values for parameter *a*, *b*, *k*, and *c*, in the SVM model

	gamma	cost
a	0.5	200
b	0.09	300
k	0.05	800
c	0.5	50

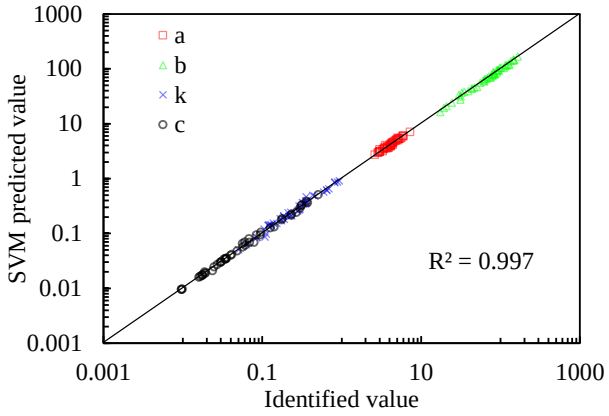

Figure 10. Correlation of the SVM estimation and identified model parameters.

However, the SVM assisted model should be further validated for test scenarios that were not used in the training process to prove the effectiveness of generalization. The hysteresis loops of MRG under strain amplitudes of 20%, 40%, 60%, and, 80%, frequencies of 0.1, 0.5, 1, and, 2 Hz, and field densities of 0, 0.27, 0.46, and 0.91 T were used as inputs for the formulated SVM-assisted model. The measured hysteresis loops and estimations from the SVM-assisted model are compared in figure 11 and 12, which suggest well agreement between the experiments (solid lines) and the prediction (dotted lines). Figure 11 (a), (b), (c) and (d) show the result for 0.64 T scenario under the frequencies of 0.1, 0.5, 1, and 2 Hz, respectively; In each of these four plots, hysteresis loops under different strain amplitudes (20%, 40%, 60%, and, 80%) are compared. The ideal fitting between the experimental data and the results from the SVM assisted model suggests that the proposed model is capable of describing the effects of both excitation frequency and strain amplitude for MRG. The effectiveness of the SVM assisted model of depicting the influence of magnetic fields is presented in Figure 12, for 20% strain and 2 Hz frequency; and, the model traced the experimental results closely for all magnetic fields considered. These results suggested that the proposed SVM-assisted model can accurately describe the hysteretic behaviour under the influences of frequency, strain amplitude, and, magnetic field for MRG; and, the application of SVM in the model for generalization purpose is practical.

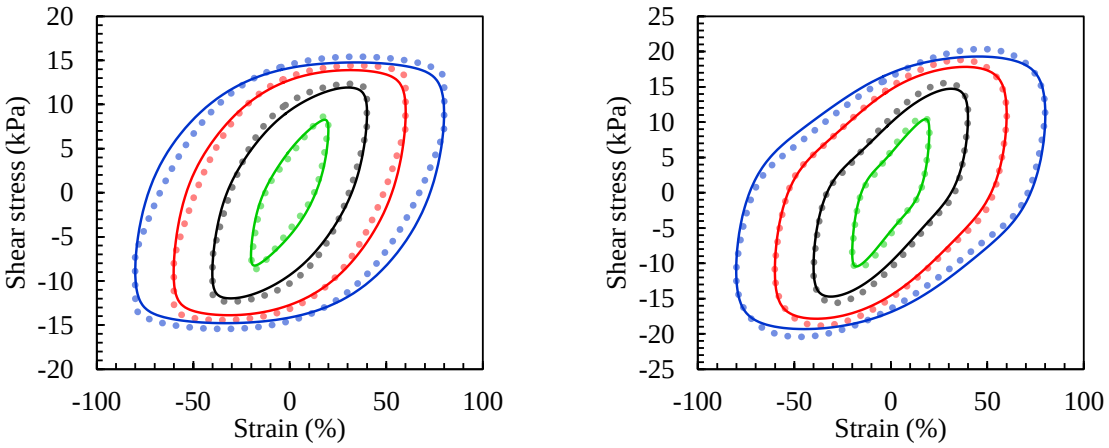

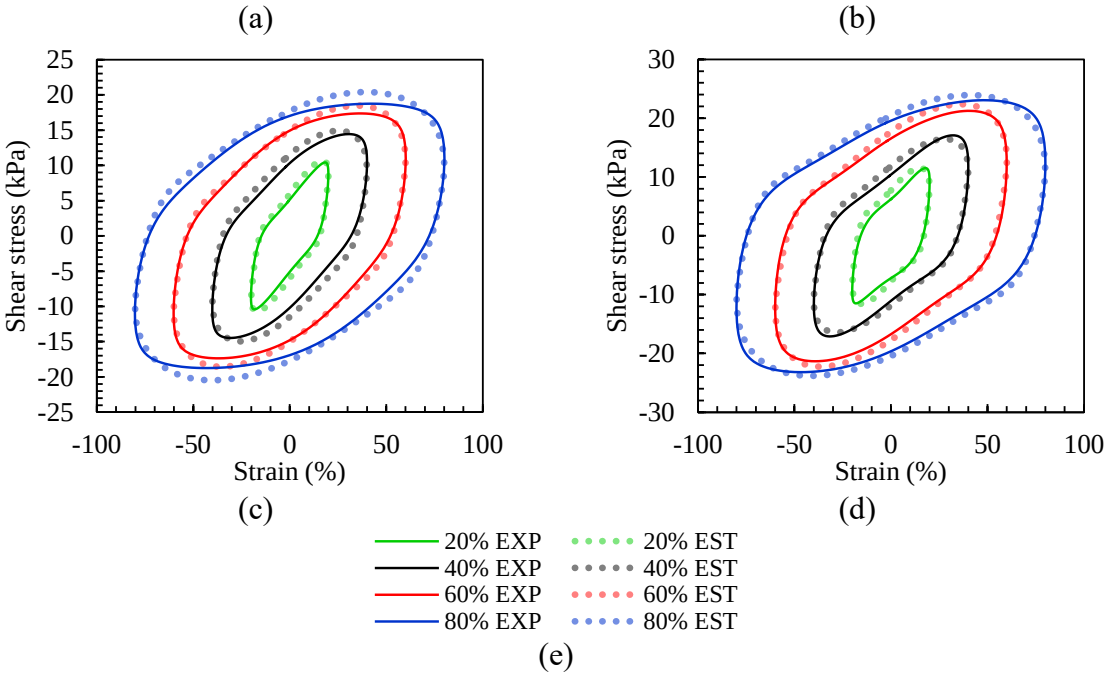

Figure 11. Comparison between experimental data and results from the SVM assisted model result for 20%, 40%, 60%, 80% strain when 0.64 T applied (a) 0.1 Hz; (b) 0.5 Hz; (c) 1 Hz; (d) 2 Hz; (e) the legend for figure 11(a) to (d).

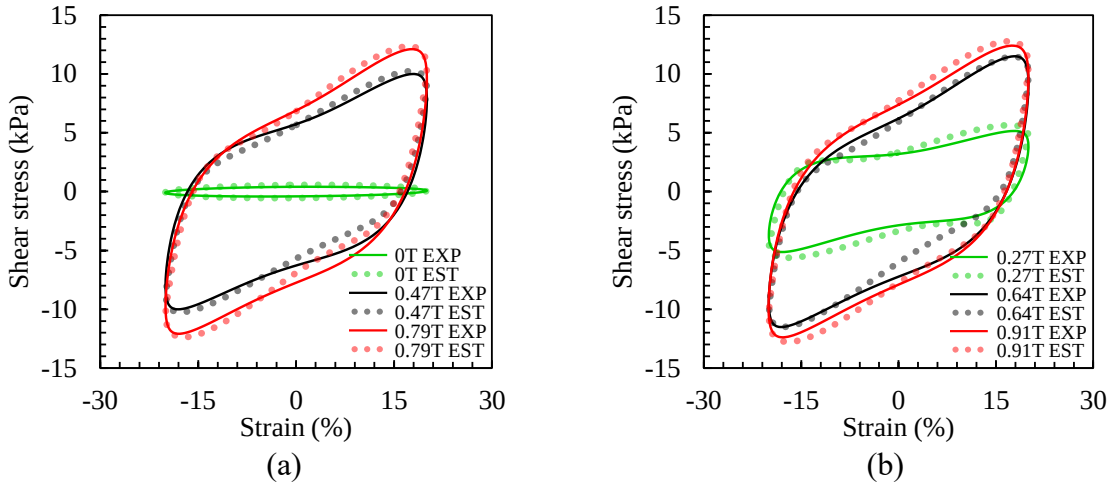

Figure 12. Comparison between experimental data and results from the SVM assisted model result for 20%, 2Hz when (a) 0, 0.47, 0.79 T applied; (b) 0.27, 0.64, 0.91 T applied.

4. Conclusion

As a recently developed controllable material, MRG exhibits high adjustability in the material properties and excels in the sedimentation performance which can benefit the development of controllable devices. However, the nonlinearities of MRG under the application of different levels of the magnetic field is unique from other controllable materials, i.e., MRF and MRE. Moreover, in the characterized stress-strain hysteresis loops, clear overshoot of shear stress was observed at the reverse of shear flow when low magnetic field applied (0.27 T). The occurrence of this phenomenon could cause severe instability and false control feedback of adaptive devices.

This research characterized its dynamic hysteresis performances under a broad band of excitations and external magnetic field to take the full advantages of MRG and achieve

precision control of the adaptive devices. A simple and accurate four-parameter phenomenological model was proposed and validated with the characterized hysteresis data of MRG. This model is based on the variation of a classic Kelvin-Voigt model with adding a proposed overshoot element. The proposed phenomenological model showed good agreement with experimental data; and, its identified parameters were analysed for the dependencies on the magnetic field and excitation inputs. By implementing SVM to the proposed phenomenological model, an SVM assisted model was formed and showed excellence in tracing the stress-strain performances of MRG under all the excitation frequency, strain amplitude, and magnetic field considered. And the magnitude and location of stress overshoot under a low magnetic field were also accurately described. These results proved that the proposed models have the effectiveness of predicting the dynamic hysteresis behaviours for MRG under varying magnetic fields and excitations; and, the applicability of employing in the control algorithms.

5. CRediT Authorship Contribution Statement

SL: Methodology, Software, Formal analysis, Investigation, data curation, Writing – Original draft. TT: Investigation. HW: Investigation. YL: Conceptualization, Validation, Resources, Writing – Review & Editing, Supervision, project administration, funding acquisition. JL: Supervision, project administration, funding acquisition. YZ: Project administration, funding acquisition. JW: Writing – Review & Editing.

6. Data Availability

The data is available upon request and please contact the corresponding author to access the data.

Reference

1. Khayam, S. U., Usman, M., Umer, M. A., & Rafique, A. (2020). Development and characterization of a novel hybrid magnetorheological elastomer incorporating micro and nano size iron fillers. *Materials & Design*, 108748.
2. Bastola, A. K., Hoang, V. T., & Li, L. (2017). A novel hybrid magnetorheological elastomer developed by 3D printing. *Materials & Design*, *114*, 391-397.
3. Zhang, L., Huang, Z., Shao, H., Li, Y., & Zheng, H. (2016). Effects of γ-Fe2O3 on γ-Fe2O3/Fe3O4 composite magnetic fluid by low-temperature low-vacuum oxidation method. *Materials & Design*, *105*, 234-239.
4. Hu, T., Xuan, S., Ding, L., & Gong, X. (2018). Stretchable and magneto-sensitive strain sensor based on silver nanowire-polyurethane sponge enhanced magnetorheological elastomer. *Materials & Design*, *156*, 528-537.
5. Mitsumata, T., & Abe, N. (2009). Magnetic-field sensitive gels with wide modulation of dynamic modulus. *Chemistry letters*, *38*(9), 922-923.
6. Yang, P., Yu, M., Fu, J., & Luo, H. (2018). Rheological properties of dimorphic magnetorheological gels mixed dendritic carbonyl iron powder. *Journal of Intelligent Material Systems and Structures*, *29*(1), 12-23.
7. Ashtiani, M., Hashemabadi, S. H., & Ghaffari, A. (2015). A review on the magnetorheological fluid preparation and stabilization. *Journal of magnetism and Magnetic Materials*, *374*, 716-730.
8. An, H. N., Picken, S. J., & Mendes, E. (2012). Direct observation of particle rearrangement during cyclic stress hardening of magnetorheological gels. *Soft Matter*, *8*(48), 11995-12001.
9. Hu, B., Fuchs, A., Huseyin, S., Gordaninejad, F., & Evrensel, C. (2006). Supramolecular magnetorheological polymer gels. *Journal of applied polymer science*, *100*(3), 2464-2479.
10. Wu, J., Gong, X., Fan, Y., & Xia, H. (2011). Physically crosslinked poly (vinyl alcohol) hydrogels with magnetic field controlled modulus. *Soft Matter*, *7*(13), 6205-6212.

11. Mitsumata, T., Sakai, K., & Takimoto, J. I. (2006). Giant reduction in dynamic modulus of κ-carrageenan magnetic gels. *The Journal of Physical Chemistry B*, *110*(41), 20217-20223.
12. Liu, B., Du, C., Yu, G., & Fu, Y. (2019). Shear thickening effect of a multifunctional magnetorheological gel: the influence of cross-linked bonds and solid particles. *Smart Materials and Structures*, *29*(1), 015004.
13. An, H. N., Sun, B., Picken, S. J., & Mendes, E. (2012). Long time response of soft magnetorheological gels. *The Journal of Physical Chemistry B*, *116*(15), 4702-4711.
14. Xu, Y., Gong, X., & Xuan, S. (2013). Soft magnetorheological polymer gels with controllable rheological properties. *Smart Materials and Structures*, *22*(7), 075029.
15. Wei, B., Gong, X., Jiang, W., Qin, L., & Fan, Y. (2010). Study on the properties of magnetorheological gel based on polyurethane. *Journal of applied polymer science*, *118*(5), 2765-2771.
16. Fuchs, A., Xin, M., Gordaninejad, F., Wang, X., Hitchcock, G. H., Gecol, H., ... & Korol, G. (2004). Development and characterization of hydrocarbon polyol polyurethane and silicone magnetorheological polymeric gels. *Journal of applied polymer science*, *92*(2), 1176-1182.
17. An, H., Picken, S. J., & Mendes, E. (2012). Nonlinear rheological study of magneto responsive soft gels. *Polymer*, *53*(19), 4164-4170.
18. Dargahi, A., Rakheja, S., & Sedaghati, R. (2019). Development of a field dependent Prandtl-Ishlinskii model for magnetorheological elastomers. *Materials & Design*, *166*, 107608.
19. Li, S., Liang, Y., Li, Y., Li, J., & Zhou, Y. (2020). Investigation of dynamic properties of isotropic and anisotropic magnetorheological elastomers with a hybrid magnet shear test rig. *Smart Materials and Structures*.
20. Gong, X., Xu, Y., Xuan, S., Guo, C., Zong, L., & Jiang, W. (2012). The investigation on the nonlinearity of plasticine-like magnetorheological material under oscillatory shear rheometry. *Journal of Rheology*, *56*(6), 1375-1391.
21. Li, W. H., Zhou, Y., & Tian, T. F. (2010). Viscoelastic properties of MR elastomers under harmonic loading. *Rheologica acta*, *49*(7), 733-740.
22. Goncalves, F. D., Koo, J. H., & Ahmadian, M. (2006). A review of the state of the art in magnetorheological fluid technologies—Part I: MR fluid and MR fluid models. *The Shock and Vibration Digest*, *38*(3), 203-220.
23. Gandhi, F., & Bullough, W. A. (2005). On the phenomenological modeling of electrorheological and magnetorheological fluid preyield behaviour. *Journal of Intelligent Material Systems and Structures*, *16*(3), 237-248.
24. Davis, L. C. (1999). Model of magnetorheological elastomers. *Journal of Applied Physics*, *85*(6), 3348-3351.
25. Zhang, X., Li, W., & Gong, X. L. (2008). An effective permeability model to predict field-dependent modulus of magnetorheological elastomers. *Communications in Nonlinear Science and Numerical Simulation*, *13*(9), 1910-1916.
26. Guo, Z., Chen, Y., Wan, Q., Li, H., Shi, X., Tang, S., & Peng, X. (2016). A hyperelastic constitutive model for chain-structured particle reinforced neo-Hookean composites. *Materials & Design*, *95*, 580-590.
27. Yu, Y., Li, J., Li, Y., Li, S., Li, H., & Wang, W. (2019). Comparative investigation of phenomenological modeling for hysteresis responses of magnetorheological elastomer devices. *International journal of molecular sciences*, *20*(13), 3216.
28. Yu, Y., Li, Y., Li, J., & Gu, X. (2016). A hysteresis model for dynamic behaviour of magnetorheological elastomer base isolator. *Smart Materials and Structures*, *25*(5), 055029.

29. Spencer Jr, B., Dyke, S. J., Sain, M. K., & Carlson, J. (1997). Phenomenological model for magnetorheological dampers. *Journal of engineering mechanics*, *123*(3), 230-238.
30. Yang, G., Spencer Jr, B. F., Jung, H. J., & Carlson, J. D. (2004). Dynamic modeling of large-scale magnetorheological damper systems for civil engineering
31. Xie, X., Xu, L., & Li, Z. (2020). Modeling of Magnetorheological Self-Centering Brace. *Journal of Engineering Mechanics*, *146*(1), 04019112.
32. Yang, J., Du, H., Li, W., Li, Y., Li, J., Sun, S., & Deng, H. X. (2013). Experimental study and modeling of a novel magnetorheological elastomer isolator. *Smart Materials and Structures*, *22*(11), 117001.
33. Wang, H., Li, Y., Zhang, G., & Wang, J. (2019). Effect of temperature on rheological properties of lithium-based magnetorheological grease. *Smart Materials and Structures*, *28*(3), 035002.
34. Sahin, H., Wang, X., & Gordaninejad, F. (2009). A new model for yield stress of magnetorheological greases/gels under combined effects of magnetic field and temperature. In *Active and Passive Smart Structures and Integrated Systems 2009* (Vol. 7288, p. 72881E). International Society for Optics and Photonics.
35. Bai, X. X., & Chen, P. (2019). On the Hysteresis Mechanism of Magnetorheological Fluids. *Front. Mater. 6: 36. doi: 10.3389/fmats*.
36. Zhang, G., Li, Y., Wang, H., & Wang, J. (2019). Rheological Properties of Polyurethane-based Magnetorheological Gels. *Front. Mater. 6: 56. Doi: 10.3389/fmats*.
37. Fuchs, A., Hu, B., Gordaninejad, F., & Evrensel, C. (2005). Synthesis and characterization of magnetorheological polyimide gels. *Journal of applied polymer science*, *98*(6), 2402-2413.
38. Ewoldt, R. H., & McKinley, G. H. (2010). On secondary loops in LAOS via self-intersection of Lissajous–Bowditch curves. *Rheologica Acta*, *49*(2), 213-219.
39. Hyun, K., Nam, J. G., Wilhelm, M., Ahn, K. H., & Lee, S. J. (2003). Nonlinear response of complex fluids under LAOS (large amplitude oscillatory shear) flow. *Korea-Australia Rheology Journal*, *15*(2), 97-105.
40. Ewoldt, R. H., Hosoi, A. E., & McKinley, G. H. (2008). New measures for characterizing nonlinear viscoelasticity in large amplitude oscillatory shear. *Journal of Rheology*, *52*(6), 1427-1458.
41. Zhou, L., Cook, L. P., & McKinley, G. H. (2010). Probing shear-banding transitions of the VCM model for entangled wormlike micellar solutions using large amplitude oscillatory shear (LAOS) deformations. *Journal of non-newtonian fluid mechanics*, *165*(21-22), 1462-1472.
42. Sim, H. G., Ahn, K. H., & Lee, S. J. (2003). Large amplitude oscillatory shear 19ehaviour of complex fluids investigated by a network model: A guideline for classification. *Journal of Non-Newtonian Fluid Mechanics*, *112*(2-3), 237-250.
43. Renou, F., Stellbrink, J., & Petekidis, G. (2010). Yielding processes in a colloidal glass of soft star-like micelles under large amplitude oscillatory shear (LAOS). *Journal of Rheology*, *54*(6), 1219-1242.
44. Divoux, T., Barentin, C., & Manneville, S. (2011). Stress overshoot in a simple yield stress fluid: An extensive study combining rheology and velocimetry. *Soft Matter*, *7*(19), 9335-9349.
45. Wang, L. X., & Kamath, H. (2006). Modelling hysteretic behaviour in magnetorheological fluids and dampers using phase-transition theory. *Smart materials and structures*, *15*(6), 1725.
46. Yang, G., Spencer Jr, B. F., Jung, H. J., & Carlson, J. D. (2004). Dynamic modeling of large-scale magnetorheological damper systems for civil engineering applications. *Journal of Engineering Mechanics*, *130*(9), 1107-1114.

47. Christensen, R. (2012). *Theory of viscoelasticity: an introduction*. Elsevier.
48. Duchon, J. (1977). Splines minimizing rotation-invariant semi-norms in Sobolev spaces. In *Constructive theory of functions of several variables* (pp. 85-100). Springer, Berlin, Heidelberg.
49. Chong, J. W., Kim, Y., & Chon, K. H. (2014). Nonlinear multiclass support vector machine–based health monitoring system for buildings employing magnetorheological dampers. *Journal of Intelligent Material Systems and Structures*, *25*(12), 1456-1468.
50. Xiong, J., Shi, S. Q., & Zhang, T. Y. (2020). A machine-learning approach to predicting and understanding the properties of amorphous metallic alloys. *Materials & Design*, *187*, 108378.
51. Zhang, Y., Hong, G. S., Ye, D., Zhu, K., & Fuh, J. Y. (2018). Extraction and evaluation of melt pool, plume and spatter information for powder-bed fusion AM process monitoring. *Materials & Design*, *156*, 458-469.
52. Konstantopoulos, G., Koumoulos, E. P., & Charitidis, C. A. (2020). Classification of mechanism of reinforcement in the fiber-matrix interface: Application of Machine Learning on nanoindentation data. *Materials & Design*, 108705.

Appendix

Measured hysteresis for MRG and modelling results of the proposed model

Excitation frequency=0.1 Hz

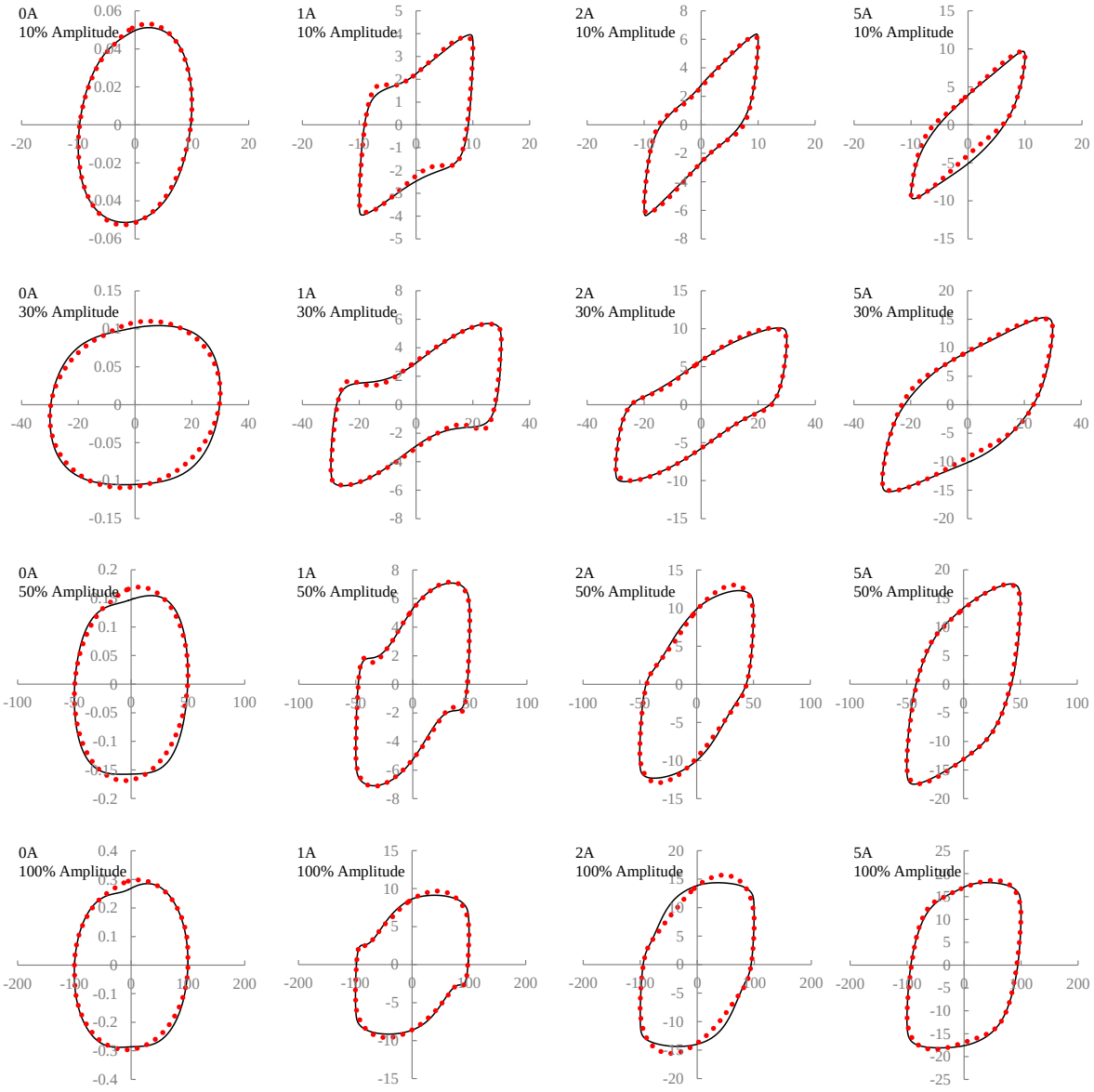

Note:

Horizontal axis: strain amplitude (%); vertical axis: shear stress (kPa); black solid line: experimental data; red dotted line: predicted results from the proposed model.

Excitation frequency=0.5 Hz

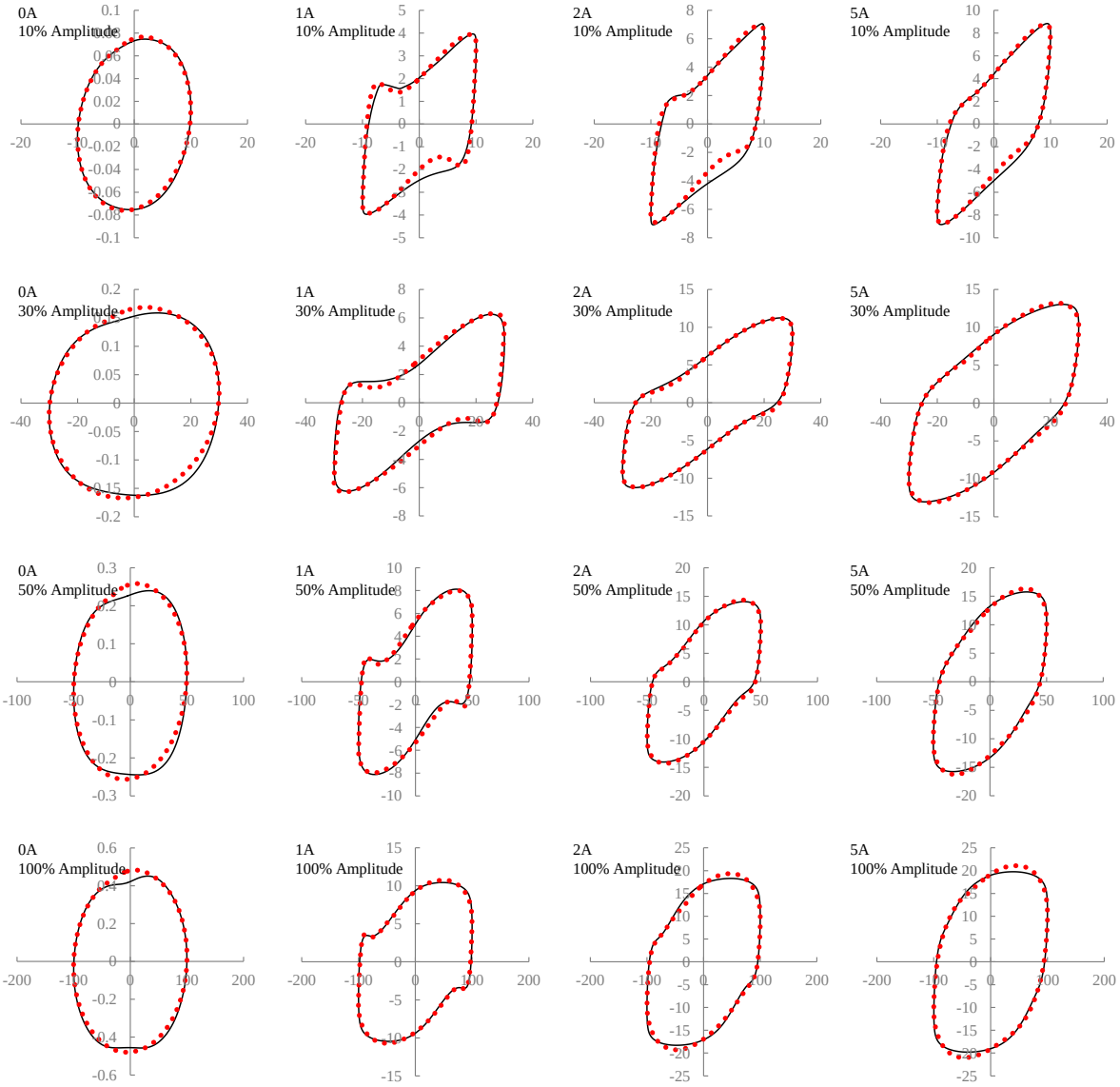

Note:

Horizontal axis: strain amplitude (%); vertical axis: shear stress (kPa); black solid line: experimental data; red dotted line: predicted results from the proposed model.

Excitation frequency=1 Hz

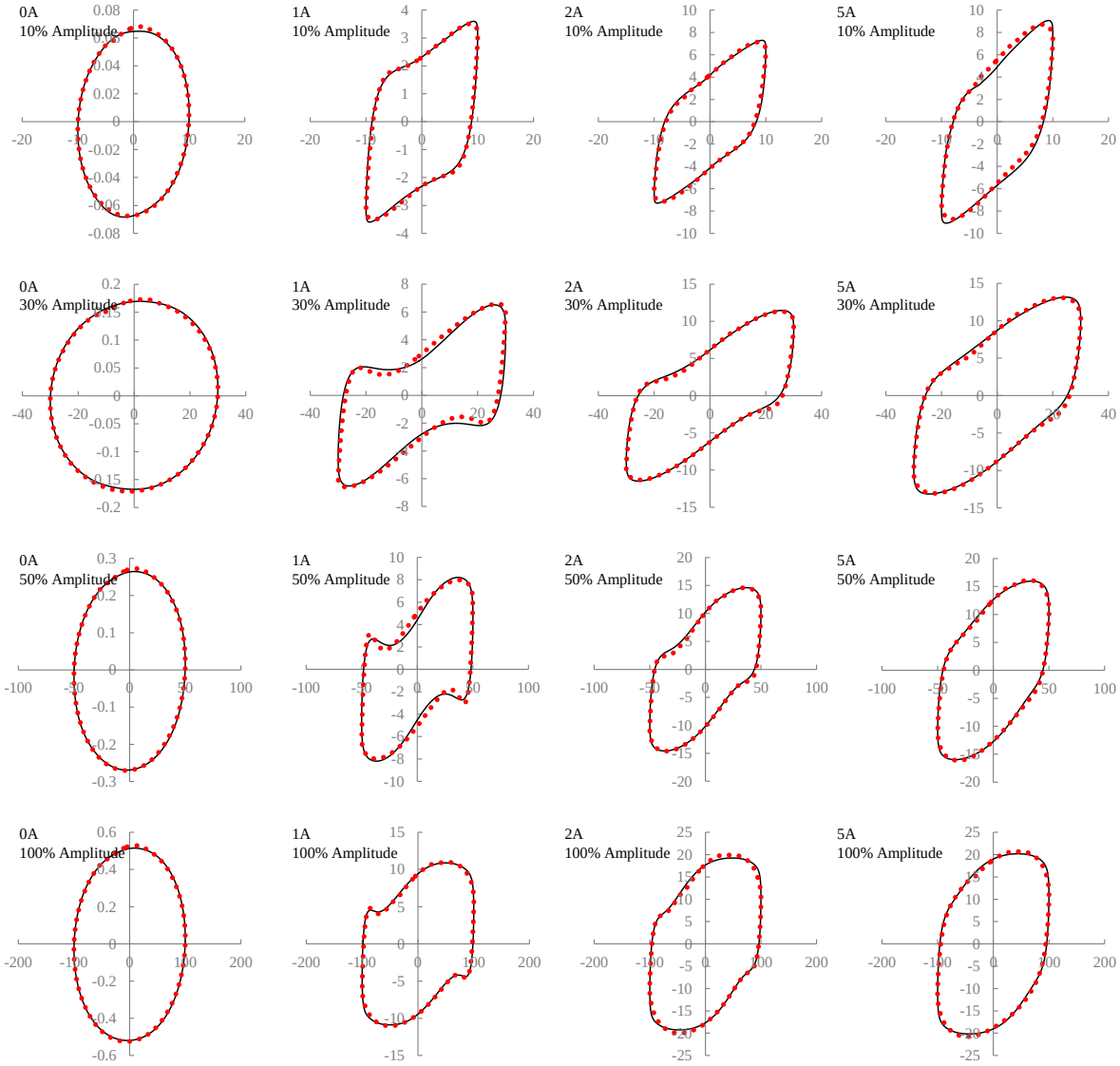

Note:

Horizontal axis: strain amplitude (%); vertical axis: shear stress (kPa); black solid line: experimental data; red dotted line: predicted results from the proposed model.

Excitation frequency=2 Hz

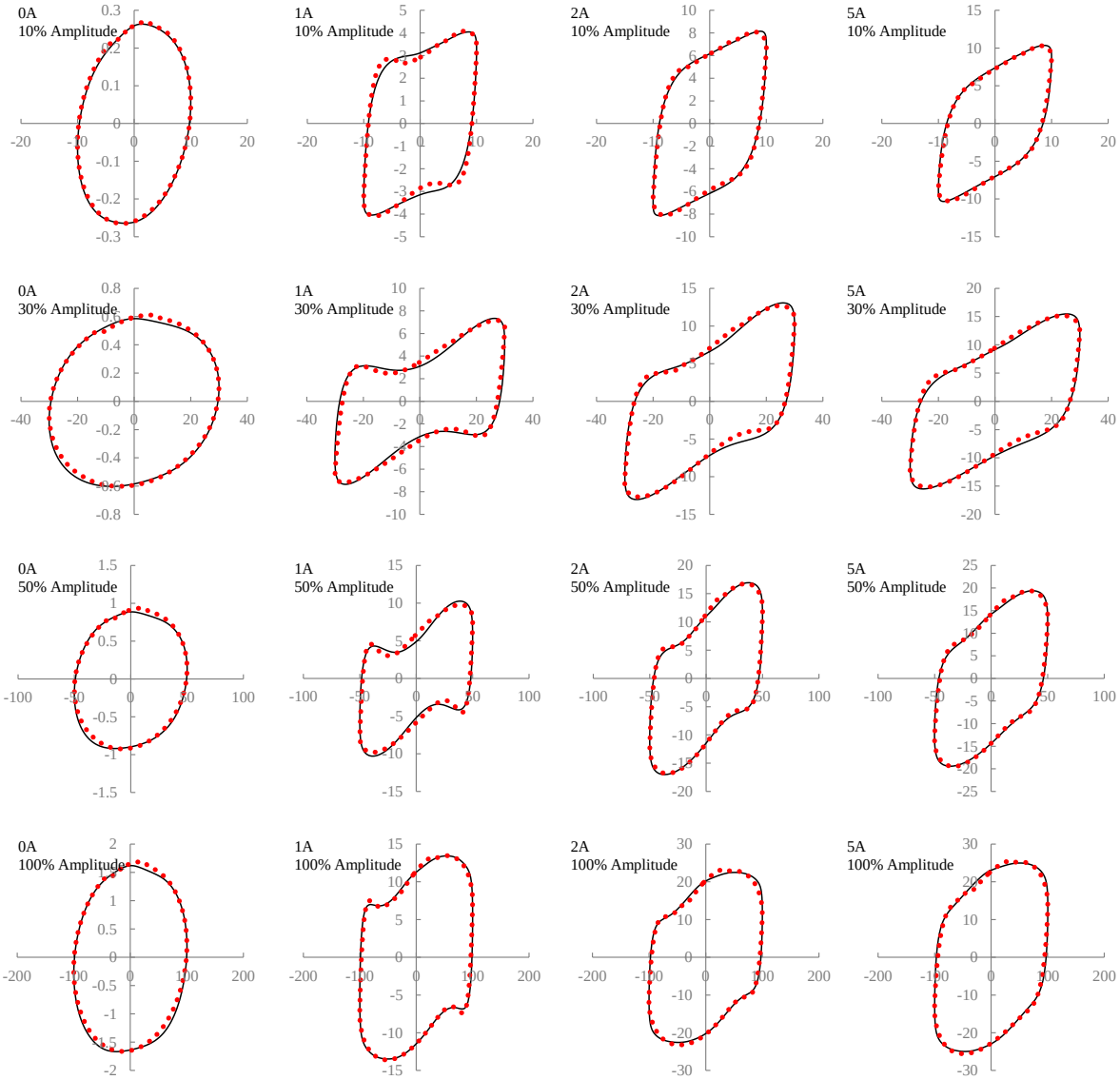

Note:

Horizontal axis: strain amplitude (%); vertical axis: shear stress (kPa); black solid line: experimental data; red dotted line: predicted results from the proposed model.